J. Fluid Mech. (2021), *vol*. 918, A26, doi:10.1017/jfm.2021.341

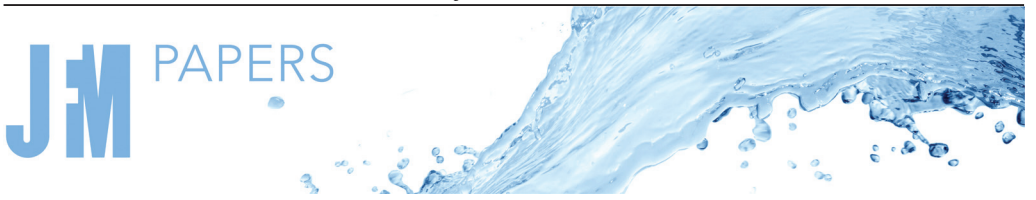

Barotropic to baroclinic energy conversion using a time-varying background density

Sorush Omidvar[1],†, **Mohammadreza Davoodi**[2] **and C. Brock Woodson**[1]

[1]School of Environmental, Civil, Agricultural, and Mechanical Engineering, University of Georgia, Athens, GA 30602, USA

[2]UT Arlington Research Institute, University of Texas at Arlington, Fort Worth, TX 76118, USA

(Received 20 August 2020; revised 25 February 2021; accepted 12 April 2021)

Internal wave generation is fundamentally the conversion of barotropic to baroclinic energy that often occurs due to vertical acceleration of stratified flows over topographic features. Acceleration results in a phase lag between density (pressure) perturbations and the barotropic velocity. To estimate the conversion of barotropic to baroclinic energy, the density perturbation is often calculated using a time-invariant background density. Other phenomena, however, can also alter the phasing of density perturbations and vertical velocities, such as barotropic tidal heaving and internal wave interactions. Consequently, accurately accounting for these dynamics in energy budgets is important. Tidal averaging or modal decomposition are often used to isolate topographic energy conversion in the presence of these other phenomena. However, while effective, these methods do not provide insights into the dynamics of conversion either through time or over depth. Here, we present a new analytical approach to calculating barotropic to baroclinic conversion using a time-varying background density. Our method results in an additional term in the baroclinic energy budget that directly accounts for barotropic tidal heaving and internal wave interactions, depending on the formulation of the background density. The tidally averaged, domain-integrated conversion rate is consistent across methods. Isolation of topographic conversion demonstrates that conversion due to interactions between internal wave beams and barotropic tidal heaving lead to relatively small differences in the overall conversion. However, using a time-varying background density allows for full decomposition of barotropic to baroclinic conversion through time and the identification of regions where negative conversion related to mixing actually occurs.

Key words: coastal engineering, internal waves, ocean processes

† Email address for correspondence: sorush.omidvar@gmail.com

1. Introduction

Internal waves (IWs), propagating through density-stratified media in a rotating frame of reference, are common features in the ocean which affect circulation and are believed to close the ocean energy budget by dissipating approximately 25 % to 30 % of tidal energy (Garrett & Munk 1979; Munk & Wunsch 1998; Egbert & Ray 2000). Consequently, IW generation and propagation have received considerable focus over the past several decades (Rattray 1960; Bell 1975; Baines 1982). IWs, particularly internal tides, are often generated through the vertical acceleration of tidal currents over a sloping topography (i.e. ridges or continental shelf breaks) causing vertical fluctuations of isopycnals (Rattray 1960; Baines 1974; Bell 1975; Holloway & Merrifield 1999; Merrifield & Holloway 2002; Klymak *et al.* 2006). To quantify IW generation due to flow–topography interactions, the conversion rate (C) of barotropic (BT) to baroclinic (BC) energy is often used (Merrifield, Holloway & Johnston 2001; Venayagamoorthy & Fringer 2005; Lamb 2007; Moum *et al.* 2007; Kang & Fringer 2010, 2012; Lien *et al.* 2014; Palmer *et al.* 2015). The value of C is commonly estimated using a time-invariant background density profile, and then averaged over a tidal cycle to estimate topographic conversion (Kang & Fringer 2012; Müller 2013). These methods provide reliable estimates of C due to flow over topography. However, they are generally limited to linear waves and do not provide insight into the evolution and dynamics of BT to BC energy conversion through time, or due to other processes such as vertical fluid displacements caused by tides and other IWs. Here, we introduce a dynamic decomposition of the BC energy budget that accurately accounts for BT tidal heaving (BTH) using a time-varying background density, allows for investigation of the conversion dynamics through time or over depth and is not limited to linear IWs.

The value of C depends on the density (pressure) perturbation, the BT velocity and the topographic slope. In the absence of a sloping ocean bottom, tides lead to vertical displacement of the water surface and constant density surfaces (isopycnals) with associated vertical velocities. The phase difference between the displacement of isopycnals and vertical velocity leads to BT–BC conversion that sums to zero over a tidal cycle. Thus, in the absence of a sloping topography, a stratified fluid heaves up and down without a net conversion of energy to other modes. However, IWs can interact with BTH, which results in energy conversion that is not due to flow–topography interaction. In addition to BTH, the presence of remotely generated IWs in coastal regions can affect IW generation when tides and remotely generated waves are phase locked (Kelly & Nash 2010; Zilberman *et al.* 2011; Nash *et al.* 2012; Pickering *et al.* 2015). Finally, IWs can interact with each other scattering energy back to BT or into other BC modes. We refer collectively to these additional sources of conversion (tide–wave, $IW \times BTH$, and wave–wave, $IW \times IW$, interactions) as 'residual conversion' as they are extraneous to, but may affect estimates of, topographic conversion. Accurate accounting of these types of conversion also allows for investigations of these interactions.

In order to estimate the topographic conversion, it is important to recognize and partition the density (pressure) perturbations effectively to isolate the conversion induced by local flow–topography interaction. Llewellyn, Stefan & Young (2002) discarded the nonlinear advection and dissipation terms in the Boussinesq momentum equations which resulted in $C = p'|_{z=-H}\boldsymbol{U}\cdot\nabla H$ (hereinafter the LSY method) where p', $\boldsymbol{U}$ and H are pressure perturbation, BT horizontal velocity and ocean bottom. This method has been widely used in the literature (Kurapov *et al.* 2003; Gerkema, Lam & Maas 2004; Carter *et al.* 2008; Kelly & Nash 2010; Kelly, Nash & Kunze 2010; Pickering *et al.* 2015). The LSY method partially removes residual conversion through the topographic slope term. Kang & Fringer (2012) included nonlinear

advection and dissipation terms to arrive at $C = \rho' g W$ (where ρ', g and W are density perturbation, gravitational acceleration, and BT vertical velocity), and removed residual conversion through tidal averaging. To filter the residual conversion, others (Lu, Wright & Brickman 2001; Kunze *et al.* 2002; Zilberman *et al.* 2011) used an approximation for the linear IW potential energy and removed the BT vertical displacement caused by surface tides over a sloping topography as approximated by Baines (1982). Kelly *et al.* (2010) developed a method based on modal decomposition to account for BTH and IW interactions. Pollmann *et al.* (2019) further proposed a semi-analytical method which gives a positive definite conversion field for linear IWs over a subcritical bathymetry through spatial smoothing. These methods, however, are generally based on a constant (time-invariant) background density (CBD), disregard nonlinear advection terms (in some cases, diffusion–dissipation terms are also neglected, except see Kang & Fringer 2012), which limits the scope of these analyses to linear IWs, and are predicated on tidal averaging to remove residual conversion. Tidal averaging, while effective, prevents the investigation of the dynamics of IW generation and BT–BC conversion at short time scales (e.g. over a tidal cycle).

Here, we directly account for BTH using a time-varying background density (TVBD). The concept of TVBD has been previously applied to study mixing (MacCready & Giddings 2016; Dossmann *et al.* 2017), but has not been used to study IW generation. We build on the formulation offered by Kang & Fringer (2012) $C = \rho' g W$ (hereinafter the KF method) by decomposing the Reynolds-averaged Navier–Stokes equations while retaining the nonlinear advection and dissipation terms. This implementation results in a new term in the BC energy budget that represents $IW \times BTH$ conversion, and conversion associated with IW reflection depending on how the TVBD is formulated. We show that this term accurately accounts for $IW \times BTH$ conversion using a background density that changes due to tides. We also show that ρ_b must be modified beyond accounting for BTH in order to isolate the effects of $IW \times IW$ conversion using an idealized three-dimensional (3-D) set-up. We develop the theoretical framework in § 2. In § 3, we outline the numerical model set-up. We discuss the application of the theoretical framework and interpret the results in § 4, and conclude the paper with a summary in § 5.

2. Theoretical framework

Under the Boussinesq approximation, conservation of mass and the Reynolds-averaged Navier–Stokes equations are

$$\nabla \cdot \boldsymbol{u} = 0, \tag{2.1}$$

$$\frac{\partial u}{\partial t} + (\boldsymbol{u} \cdot \nabla) u - f v = -\frac{1}{\rho_0}\frac{\partial P}{\partial x} + \nabla \cdot (\nu_h \nabla_h u) + \frac{\partial}{\partial z}\left(\nu_v \frac{\partial u}{\partial z}\right), \tag{2.2}$$

$$\frac{\partial v}{\partial t} + (\boldsymbol{u} \cdot \nabla) v + f u = -\frac{1}{\rho_0}\frac{\partial P}{\partial y} + \nabla \cdot (\nu_h \nabla_h v) + \frac{\partial}{\partial z}\left(\nu_v \frac{\partial v}{\partial z}\right), \tag{2.3}$$

$$\frac{\partial w}{\partial t} + (\boldsymbol{u} \cdot \nabla) w = -\frac{1}{\rho_0}\frac{\partial P}{\partial z} + \nabla \cdot (\nu_h \nabla_h w) + \frac{\partial}{\partial z}\left(\nu_v \frac{\partial w}{\partial z}\right) - \frac{\rho}{\rho_0} g, \tag{2.4}$$

where u, v, w, P, f, ν_h and ν_v are velocity in x, y and z directions, pressure, the Coriolis frequency, and the horizontal and vertical eddy viscosities, respectively. Pressure and density are partitioned into reference, background and perturbation components, and

velocities are decomposed into BT and BC components

$$\rho = \rho_0 + \rho_b + \rho', \tag{2.5}$$

$$P = P_0 + P_b + P' = g\int_z^\eta \left(\rho_0 + \rho_b(z') + \rho'(z')\right) \mathrm{d}z', \tag{2.6}$$

$$\boldsymbol{U_h} = \frac{1}{H}\int_{-d}^{\eta} \boldsymbol{u_h} = \frac{1}{H}\overline{\boldsymbol{u_h}}\,\mathrm{d}, \tag{2.7}$$

$$\boldsymbol{\nabla}\cdot\boldsymbol{U} = 0, \tag{2.8}$$

$$\boldsymbol{\nabla}\cdot\boldsymbol{u'} = 0, \tag{2.9}$$

where the $\boldsymbol{h}$ subscript denotes the horizontal (x, y and u, v), $H = \eta + d$ is the water column depth (η and $-d$ are sea surface height and ocean bottom, respectively), the bar operator provides the depth-integrated value of a parameter ($\bar{\psi} = \int_{-d}^{\eta} \psi \,\mathrm{d}z$) and capital letter velocities (U,V) are the BT components, while the prime velocities (u',v') are the BC constituents. The BT and BC vertical velocities can be found using the continuity equation $W = -\nabla_h \cdot (\boldsymbol{U}_h(d+z))$ and $w' = w - W$, respectively.

By using the momentum equations and applying boundary conditions (full derivation is provided in Kang (2010) and summarized in Appendix A), we get the depth-integrated BC kinetic energy (E'_K) budget

$$\frac{\partial \overline{E'_K}}{\partial t} + \boldsymbol{\nabla_h}\cdot(\overline{\boldsymbol{u_h} E'_K}) + \boldsymbol{\nabla_h}\cdot(\overline{\boldsymbol{u'_h} E_{K_{BT-BC}}}) = -\boldsymbol{\nabla_h}\cdot(\overline{\boldsymbol{u'_h} P'}) - \overline{\rho' g w'} + A_h + \overline{\boldsymbol{\nabla_h}\cdot(\nu_H \boldsymbol{\nabla_h} E'_K)} - D' - \overline{\epsilon_K}. \tag{2.10}$$

where A_h, D', ϵ_K are unclosed, drag and dissipation terms respectively.

For an incompressible density-stratified fluid, the available potential energy (E_A) is equal to the difference between the potential energy of the perturbed water column (E_P) and the minimum energy attainable thorough adiabatic motion (E_B) (Lorenz 1955; Winters *et al.* 1995). The concept of E_A has been widely used to study energy budgets in both deep and shallow water systems (Venayagamoorthy & Fringer 2005; Klymak *et al.* 2006; Scotti, Beardsley & Butman 2006; Kang & Fringer 2010, 2012). For any arbitrary density stratification, E_A can be found from (Kang & Fringer 2010, 2012)

$$E_A = E_P - E_B = g\int_{z-\delta}^{z} \left(\rho(z) - \rho_b(z') - \rho_0\right) \mathrm{d}z', \tag{2.11}$$

where δ is the BT and BC vertical displacement of isopycnals. For linear IWs in linear density-stratified media, E_A can further be approximated as (Gill 1982; Scotti *et al.* 2006; Lamb 2007)

$$E_A = \frac{\rho_0}{2} N^2 \delta^2 = \frac{g^2 \rho'^2}{2\rho_0 N^2}, \tag{2.12}$$

where $N^2 = -(g/\rho_0)(\partial\rho/\partial z)$ is the squared Brunt–Väisälä frequency. The E_A inside a system can be dissipated, advected or converted to kinetic energy (disregarding the spatio-temporal background density variation $\partial\rho_b/\partial x$, $\partial\rho_b/\partial y$, $\partial\rho_b/\partial t \approx 0$)

$$\overline{\frac{\partial E_A}{\partial t}} + \overline{\boldsymbol{u}\cdot\boldsymbol{\nabla} E_A} = \overline{g w \rho'(z)} + \overline{\epsilon_A}. \tag{2.13}$$

where ϵ_A is the diffusion of potential energy.

By adding (2.10) and (2.13) and tidally averaging, we get

$$\nabla_h \cdot \left\langle \overline{\boldsymbol{u} \cdot \nabla E_A} + \overline{\boldsymbol{u}_h E_k'} + \overline{\boldsymbol{u}_h' E K_{BT-BC}} + \overline{\boldsymbol{u}_h' P'} - \overline{\nu_H \nabla_h E_K'} \right\rangle = \langle \overline{\rho' g w} - \overline{\rho' g w'} \rangle + \langle A_h \rangle - \langle D' \rangle \langle \overline{\epsilon_A - \epsilon_K} \rangle, \tag{2.14}$$

where the angle bracket operator provides the tidally averaged value of a parameter over a period of T ($\langle \psi \rangle = (1/T) \int_0^T \psi \, \mathrm{d}t$). The energy conversion rate from BT to BC modes can be found by the summation of $\rho' g w$ and $-\rho' g w'$ (Kang & Fringer 2012). In such a formulation, C consists of both topographic and residual conversion. BTH of isopycnals alone (without the presence of a sloping bottom) does not generate IWs nor convert energy from BT to BC; yet, vertical acceleration over a sloping topography causes a phase lag between the density perturbation and the vertical velocity, $\phi_{\rho',W}$ (where $\phi_{a,b}$ denotes the phase difference between a and b). The conversion that occurs due to the phase lag between the density perturbation and the vertical velocity can be understood by considering two idealized sinusoidal functions assigned to ρ' and W with period, amplitude and initial phase of ω, a and b

$$\langle C \rangle = \langle \rho' g W \rangle = g \left\langle a_i \sin(\omega t + b_i) a_j \sin(\omega t + b_j) \right\rangle = g \frac{a_i a_j}{2} \cos(\phi_{b_i,b_j}) \tag{2.15}$$

leading to positive (negative) conversion rates for phase differences $< 90^\circ$ ($> 90^\circ$) (Zilberman *et al.* 2009).

To better understand how BTH contributes to conversion, we consider a system governed by tidal flows with a flat bathymetry in which isopycnals heave up (down) during flood (ebb) tides and $\phi_{W,\rho'} = 90^\circ$. Figure 1 depicts the characteristics of such a system where there are non-zero density perturbations (red curve in figure 1*c*) and BT vertical velocities (figure 1*d*) through time. The density perturbations captured by CBD methods is completely induced by BTH (compare panels (*b*) and (*c*) in figure 1). Due to the failure of BTH filtering in ρ_B a non-zero C emerges with a zero tidally averaged value (red curve in figure 1*f*) which is fully BT. By applying a proper time-varying ρ_b, the BT displacement of the background density is removed (blue curve in figure 1*c*); therefore, the residual conversion is eliminated (blue curve in figure 1*f*).

In CBD methods (e.g. both LSY and KF), ρ_b is only a function of z; while in TVBD, ρ_b is a function of z and t. The temporal dependency of ρ_b creates a new cross-term in the E_A budget which can remove arbitrary vertical displacements (a similar methodology was used by Lu *et al.* 2001; Kunze *et al.* 2002; Zilberman *et al.* 2011). By removing the BT displacement at any depth we can remove the effects of BTH. To do so, we assume that BT tidal height varies linearly over the water column as $\gamma(x, y, z, t) = \eta(1 - z/H)$.

The contribution of nonlinear advection terms in the E_A budget in the formation of $\rho' g W$ is acknowledged by Kang & Fringer (2012). Accounting for nonlinear advection terms results in an additional term in the E_A budget (see Appendix A for full derivation)

$$\overline{\frac{\partial E_A}{\partial t}} + \overline{\boldsymbol{u} \cdot \nabla E_K'} = \overline{\rho' g w} - \overline{g \int_{z-\delta}^{z} \frac{\partial \rho_b(z', t)}{\partial t} \mathrm{d}z'} + \overline{\epsilon_A}. \tag{2.16}$$

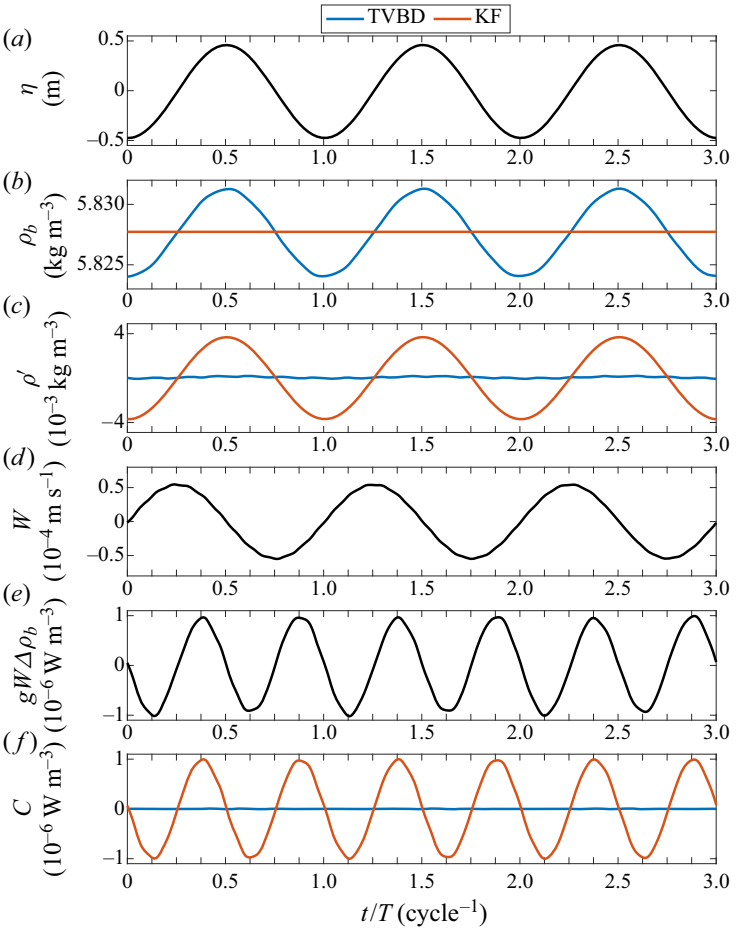

Figure 1. Times series of tidal flow over flat bottom showing (*a*) tidal height, (*b*) background density, (*c*) density perturbation, (*d*) BT vertical velocity at mid-depth, (*e*) BT conversion rate where $\Delta\rho_b$ is difference between TVBD and CBD background density and (*f*) BT–BC conversion rate.

The total energy budget (kinetic+potential), where $\langle\overline{\rho' gW - g\int_{z-\delta}^{z}(\partial\rho_b(z',t)/\partial t\,\mathrm{d}z')}\rangle$ is the modified conversion, then becomes

$$\nabla_{\boldsymbol{h}}\cdot\left\langle\overline{\boldsymbol{u}\cdot\nabla E_A}+\overline{\boldsymbol{u}_{\boldsymbol{h}}E_k'}+\overline{\boldsymbol{u}_{\boldsymbol{h}}'EK_{BT-BC}}+\overline{\boldsymbol{u}_{\boldsymbol{h}}'P'}-\overline{\nu_H\nabla_{\boldsymbol{h}}E_K'}\right\rangle$$
$$=\left\langle\overline{\rho' gW-g\int_{z-\delta}^{z}\frac{\partial\rho_b(z',t)}{\partial t}\mathrm{d}z'}\right\rangle+\langle A_h\rangle-\langle D'\rangle+\langle\overline{\epsilon_A-\epsilon_K}\rangle. \tag{2.17}$$

This formulation can be considered a modified version of Kang & Fringer (2012). The contribution of the non-hydrostatic pressure ($-\overline{(\partial q/\partial z)W}$ where q is the non-hydrostatic pressure constituent) can be added directly to this formulation (Kang & Fringer 2012). The new term in (2.17) can isolate the conversion due to the interaction of IWs and BTH ($IW\times BTH$) and even between IWs ($IW\times IW$) if the background density is formulated accordingly.

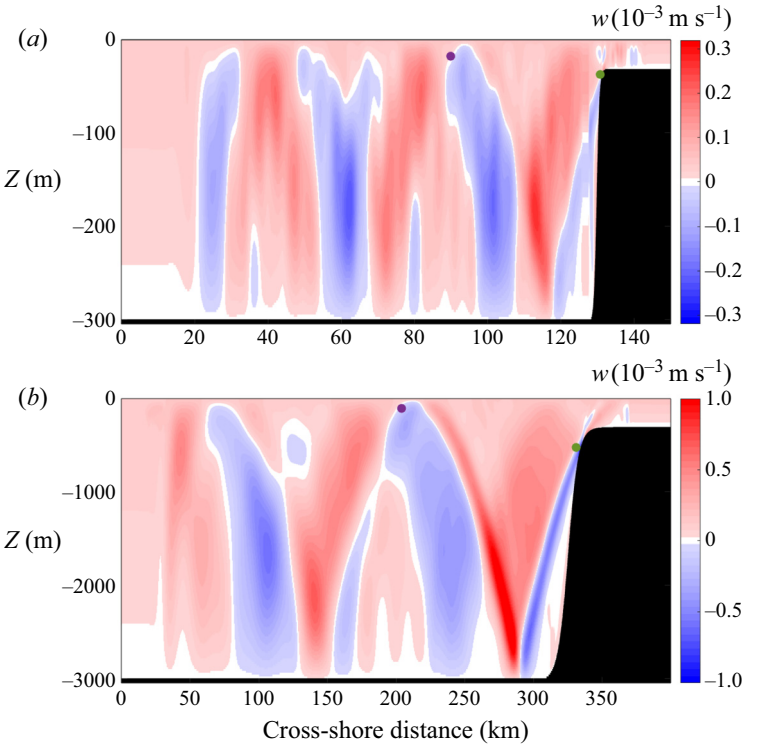

Figure 2. Vertical velocity at time $t/T = 0.4$ for (*a*) shallow (case 1) and (*b*) deep (case 2) scenarios. The generation site over the topographic feature (green circle) and a site of IW reflection from the ocean surface (purple circle) are shown.

3. Numerical set-up

To test the TVBD method and the resulting effects on C, we simulated IW generation using SUNTANS (Stanford unstructured non-hydrostatic terrain following averaged Navier–Stokes simulator). SUNTANS is a finite volume model that solves 3-D non-hydrostatic, nonlinear Navier–Stokes equations on unstructured–triangular horizontal grids with z-level vertical layers (Fringer, Gerritsen & Street 2006). SUNTANS has been widely used to study non-hydrostatic, nonlinear phenomena such as IWs and circulation in shallow coastal systems and estuaries (Jachec *et al.* 2007; Zhang, Fringer & Ramp 2011; Kang & Fringer 2012; Nelko, Saha & Chua 2014; Xu & Chua 2016). We begin our analysis with two idealized 2-D cases with high spatio-temporal resolution to highlight the TVBD method and compare it to other common methods. To validate the formulation in a more realistic set-up, we compared the results for an idealized 3-D ridge. The bathymetry for the 2-D and the 3-D set-ups can be seen in figures 2 and 3, respectively.

For all cases, we applied a constant background horizontal turbulent viscosity of $1\,\mathrm{m}^2\ \mathrm{s}^{-1}$ and employed a Mellor–Yamada 2.5 (MY 2.5) turbulence closure scheme for the vertical turbulent viscosity (Mellor & Yamada 1982). The horizontal viscosity was set to the minimum value needed to remove numerical oscillations between grid points (10 m resolution). The shortest wavelengths possible in the domain are $O(60\ \mathrm{m})$, so this did not affect IW generation. We also ran cases with $\nu_h = 0.1$, 0.01 and $0.001\ \mathrm{m}^2\ \mathrm{s}^{-1}$ and constant $\nu_v = 0.001$ and $0.0001\ \mathrm{m}^2\ \mathrm{s}^{-1}$. Results of all cases were consistent, we therefore only report cases with $\nu_h = 1\ \mathrm{m}^2\ \mathrm{s}^{-1}$ and the MY 2.5 closure scheme.

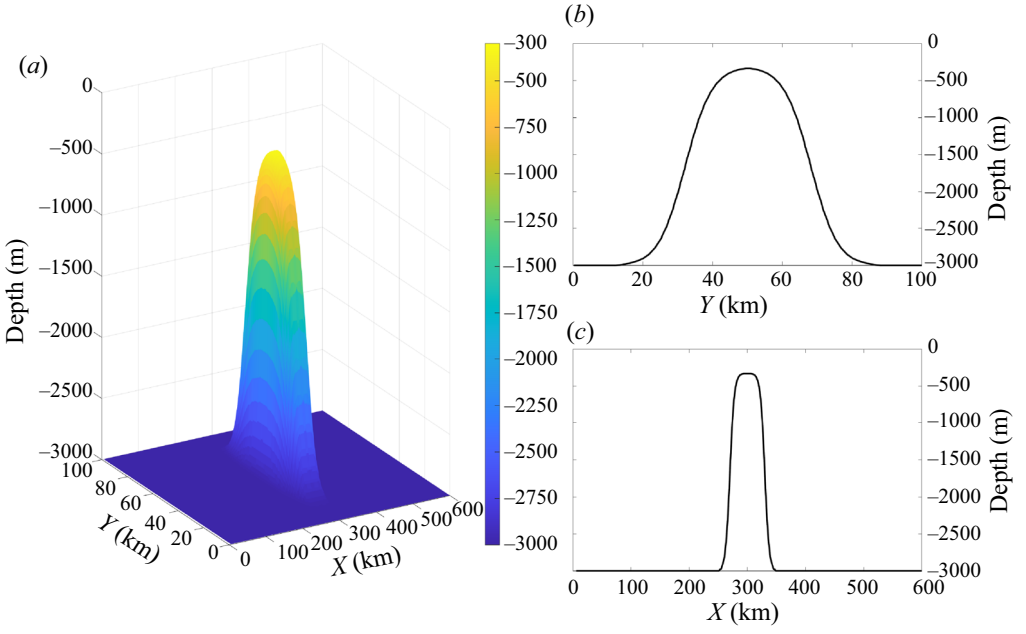

Figure 3. Ideal ridge bathymetry map (*a*, case 3) and its transects at (*b*) $X = 300$ km and (*c*) $Y = 50$ km.

To analyse the effect of depth (shallow vs deep) on C, we used idealized functions for density stratification (figure 4) and bathymetry

$$d = H_0 - 0.5(H_0 - h_0)\left(1 + \tanh\left(\frac{x - X_{mid}}{L_s}\right)\right), \tag{3.1}$$

where h_0 and H_0 are constants (minimum and maximum depths in the domain), d is the depth at any specific point, X_{mid} and L_s are bathymetric shape constants.

For all cases, M_2 tidal currents ($u = U_0 \sin(\omega t)$) were applied at the ocean-side boundary barotropically and the shore-side boundary was closed. To avoid IW reflection from offshore and onshore boundaries, u' was relaxed using a sponge layer that extended 20 km into the domain at each side. The Coriolis frequency was set to 0.8×10^{-4} s^{-1} representing ~33°N latitude. We chose this mid-latitude as it represents a value close to the region (central California) that motivated this study. However, our results were again consistent regardless of the value of f used based on additional simulations.

We examined three case scenarios (shallow 2-D shelf, deep 2-D shelf, 3-D ridge) with different physical inputs (tidal current velocity, bathymetry, eddy viscosity) and environmental parameters (domain size and spatio-temporal resolution) as summarized in table 3 in Appendix A. The models were run for 15 tidal cycles and all analyses were performed on the last 3 tidal cycles. Model set-up files and analysis scripts are available on GitHub at https://github.com/somidvar/suntans/tree/master/TVBDPaperSourceCode.

4. Results and discussion

In this section, we compare the results of CBD methods (LSY, KF) with the TVBD method and show how TVBD provides an improvement by directly allocating topographic and residual conversion. The steepness number (β_1) and tidal excursion (β_2) are informative

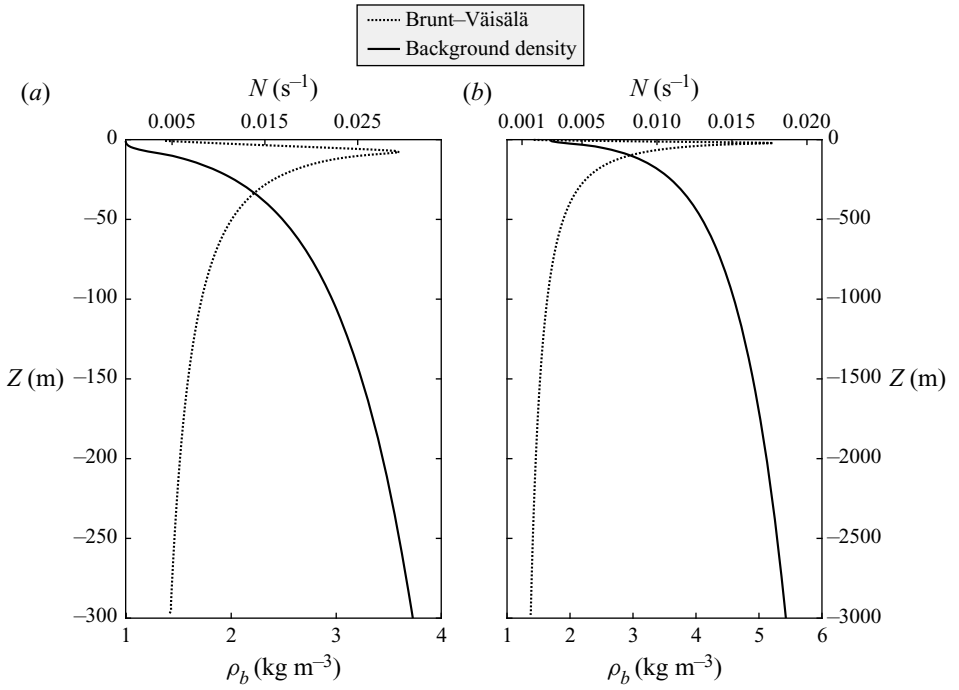

Figure 4. Background density and Brunt–Väisälä frequency at the beginning of the last 3 tidal cycles for (*a*) shallow (case 1) and (*b*) deep (cases 2 and 3) cases.

dimensionless numbers characterizing the reflectivity and period of IWs

$$\beta_1 = \frac{\tan(\theta_B)}{\tan(\theta_{IW})} = \sqrt{\frac{\left(\frac{\partial d}{\partial x}\right)^2 + \left(\frac{\partial d}{\partial y}\right)^2}{\frac{\omega^2 - f^2}{N^2 - \omega^2}}}, \tag{4.1}$$

$$\beta_2 = \frac{U_0 k_b}{\omega}, \tag{4.2}$$

where θ, U_0 and k_b^{-1} are the angle (subscripts $_B$ and $_{IW}$ denote ocean bottom and IW) with the horizontal, maximum BT tidal current velocity and topographic length scale. For IW studies, k_b is estimated as $\theta_B/(H-d)$ (Garrett & Kunze 2007; Kang & Fringer 2012). In a system with supercritical bathymetry ($\beta_1 > 1$), the majority of generated IWs propagate offshore while for a subcritical bathymetry ($\beta_1 < 1$), the IWs also move toward the shore. Tidal excursion, β_2, less than one suggests that the IW frequency is similar to the forcing frequency; while $\beta_2 > 1$ gives lee waves (Kang & Fringer 2012). For this study, all the cases have super-critical topography ($\beta_1 > 1$) and respond mainly at the perturbation frequency ($\beta_2 < 1$). To insure adequate conversion for our analyses, we set our cases with $1 < \beta_1 \leq 8$ (Kang & Fringer 2012). Therefore, we expect to see generated IWs propagating offshore as IW beams. The generated IWs can clearly be seen as elevation and depression rays as they bounce from ocean bottom and surface (figure 2).

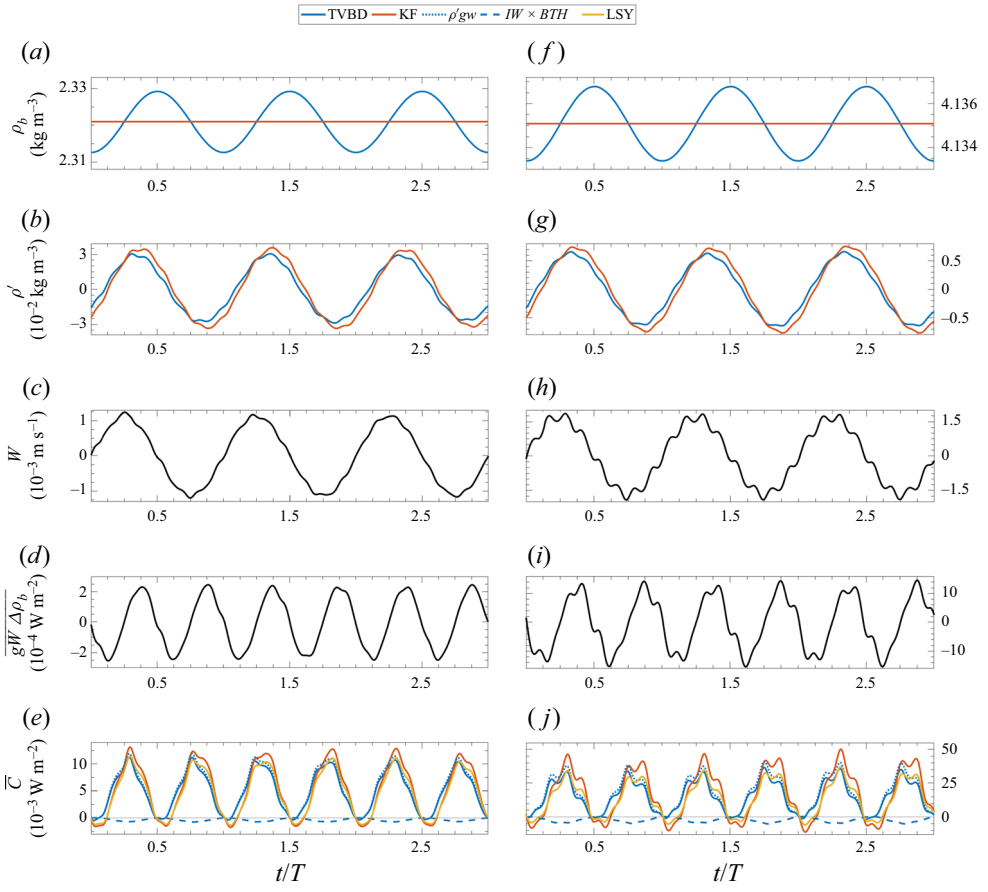

Figure 5. Time series of parameters involved in BT–BC conversion shown at generation sites (green circles in figure 2; left and right panels are for cases 1 and 2, respectively). (*a*,*f*) Background density, (*b*,*g*) perturbation density, (*c*,*h*) BT vertical velocity, (*d*,*i*) BT conversion rate where $\Delta\rho_b$ is the difference between TVBD and CBD background density and (*e*,*j*) BT–BC conversion rate as in figure 1.

4.1. *Residual conversion in time series*

The main difference between TVBD and CBD methods is the direct accounting for $IW \times BTH$ by TVBD. The conversion rate is the product of W and ρ' in which the density perturbation is induced by density changes due to BTH, vertical acceleration over a sloping bathymetry and BC oscillations. BTH results in a residual positive–negative conversion with a magnitude of $(\rho_{b_{TVBD}} - \rho_{b_{CBD}})gW$, and is responsible for the observed difference between CBD and TVBD results. Figure 5, which follows the same layout as figure 1, illustrates the difference between the two methods at the generation site (panels (*d*,*e*) and (*i*,*j*) which corresponds to 2 and 12×10^{-4} W m^{-2} for shallow and deep cases, respectively). Although the LSY method removes the background pressure P_b, this issue persists as it only removes the time-averaged background pressure P_b and not BTH. The presence of residual positive–negative conversion in the C time series shown in figures 5(*e*) and 5(*j*) supports this assertion.

4.2. *Non-zero residual conversion over flat bottom*

At reflection points, where the IWs bounce from the ocean surface and bottom, there is no active IW generation. However, residual C occurs due to disturbances caused by BTH and

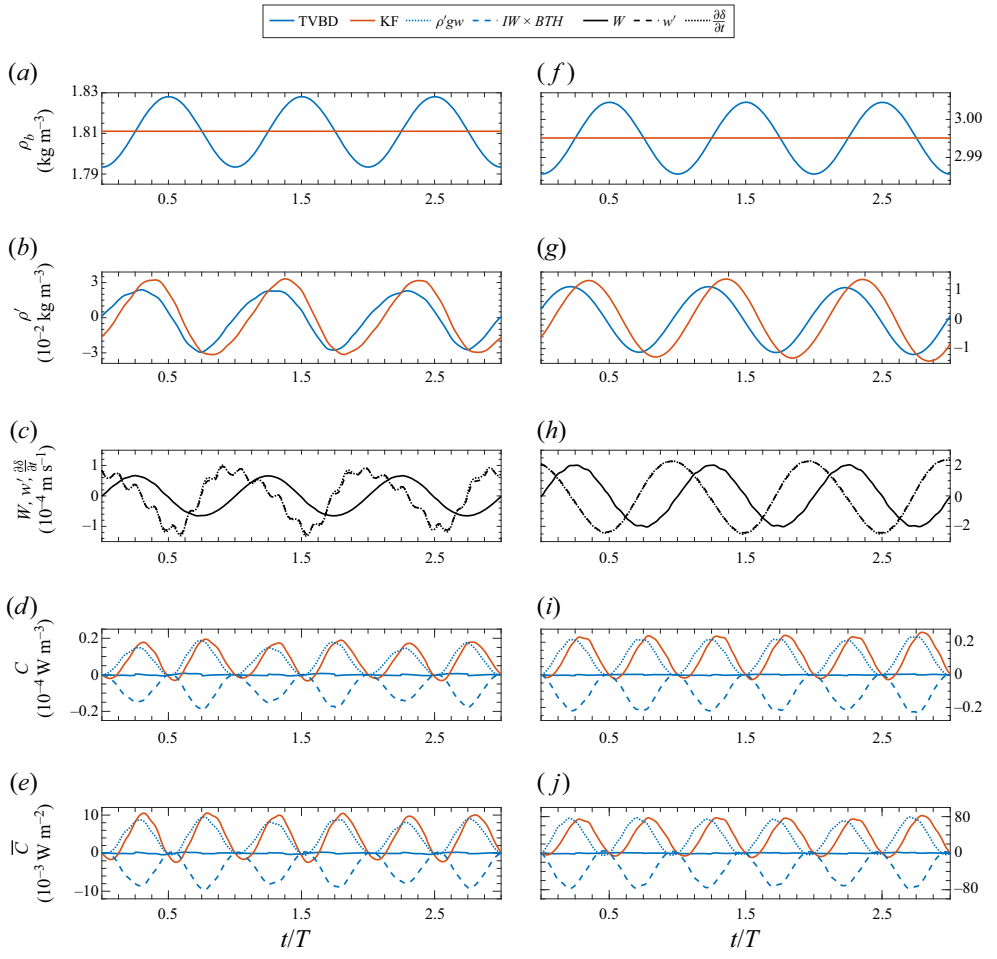

Figure 6. Time series of parameters involved in BT–BC conversion shown at reflection sites (purple circles in figure 2; left and right panels are for cases 1 and 2, respectively). (*a*,*f*) Background density, (*b*,*g*) perturbation density, (*c*,*h*) BT vertical velocity, (*d*,*i*) BT conversion rate where $\Delta\rho_b$ is the difference between TVBD and CBD background density and (*e*,*j*) BT–BC conversion rate as in figure 1.

other IWs, which is accounted for in the new interaction term of the TVBD formulation ($IW \times BTH$). Similar patterns have been reported by incoherent remotely generated IWs, which are phase locked to the surface tides by Kelly & Nash (2010), Zilberman *et al.* (2011) and Pickering *et al.* (2015). Based on Zilberman *et al.* (2009), the energy conversion is due to $\cos(\phi_{\rho',W})$, which can be affected by the presence of IWs. As shown in figure 6, the reflected IWs from the ocean surface and bottom possess w' (BC perturbations shown in (*c*,*h*)) which is not in phase with BT vertical movement; therefore, altering the phase of ρ' slightly (*b*,*g*). Conversion due to IW reflection is retained in the CBD conversion calculation as it creates residual conversion (positive or negative) away from the generation sites. Figures 7(*a*) and 7(*c*), which demonstrate the time-averaged conversion rate in the model, clearly shows the alternating shading pattern of the CBD method. In contrast, the TVBD method removes the effects of IW reflection on C through the $IW \times BTH$ term (figure 6*d*). This issue is masked in the LSY method as it depends on the topographic slope, which is zero away from the slope in this study. However, disregarding the topographic

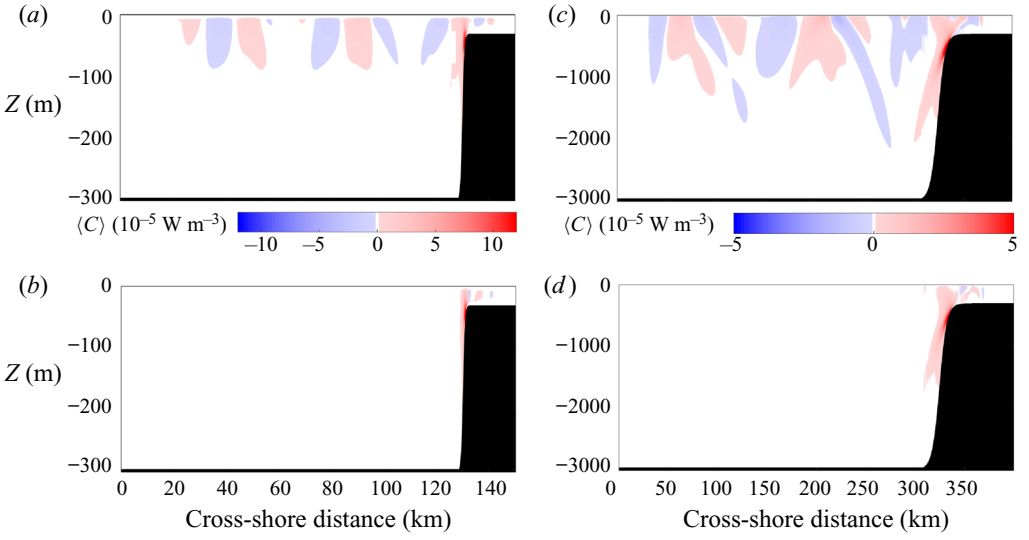

Figure 7. Time-averaged conversion rate $\langle C \rangle$ for case 1 (a,b) and case 2 (c,d) for (a,c) the KF method and (b,d) the TVBD method.

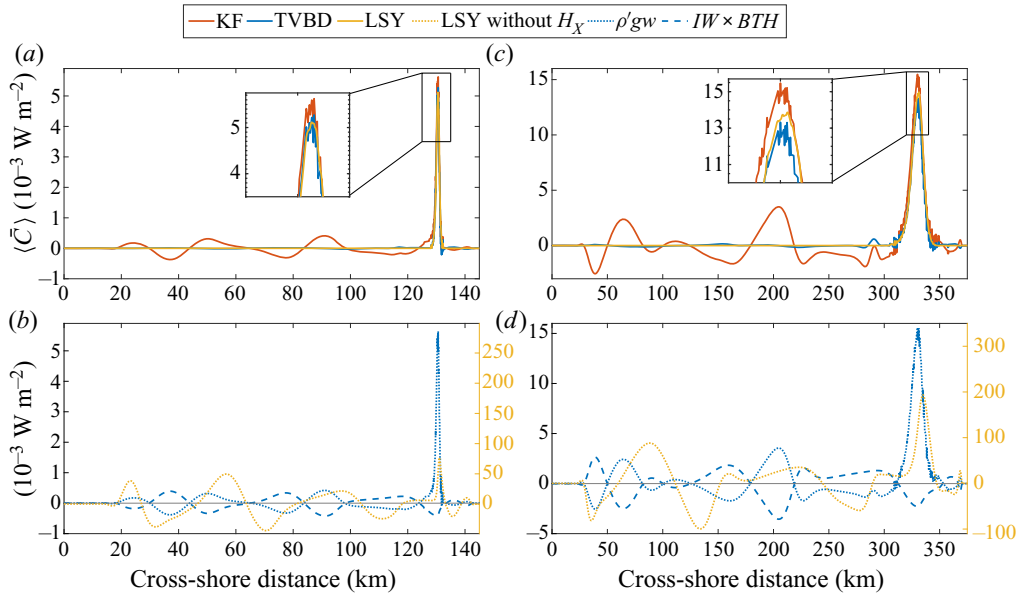

Figure 8. Time-averaged depth-integrated conversion rate ($\langle \bar{C} \rangle$) for KF, LSY and TVBD methods for shallow (a,b) and deep (c,d) cases. (a,c) A comparison between the three methods over the cross-shore model domain. (b,d) Detail of the two terms of the TVBD method and the LSY method results without the bathymetry gradient H_x.

slope in the LSY formulation ($P'|_{z=-H}\boldsymbol{U} \cdot \boldsymbol{I}$ where $I = (1, 1, 1)$ is the unity vector), we observe an oscillating pattern similar to the KF method as it retains non-zero residual conversion over the flat part of the domain. Figures 8(b) and 8(d), which provide the time-averaged depth-integrated conversion rate, show such an issue for the LSY method (panels (a) and (c) demonstrate the results of KF and TVBD methods). In real scenarios,

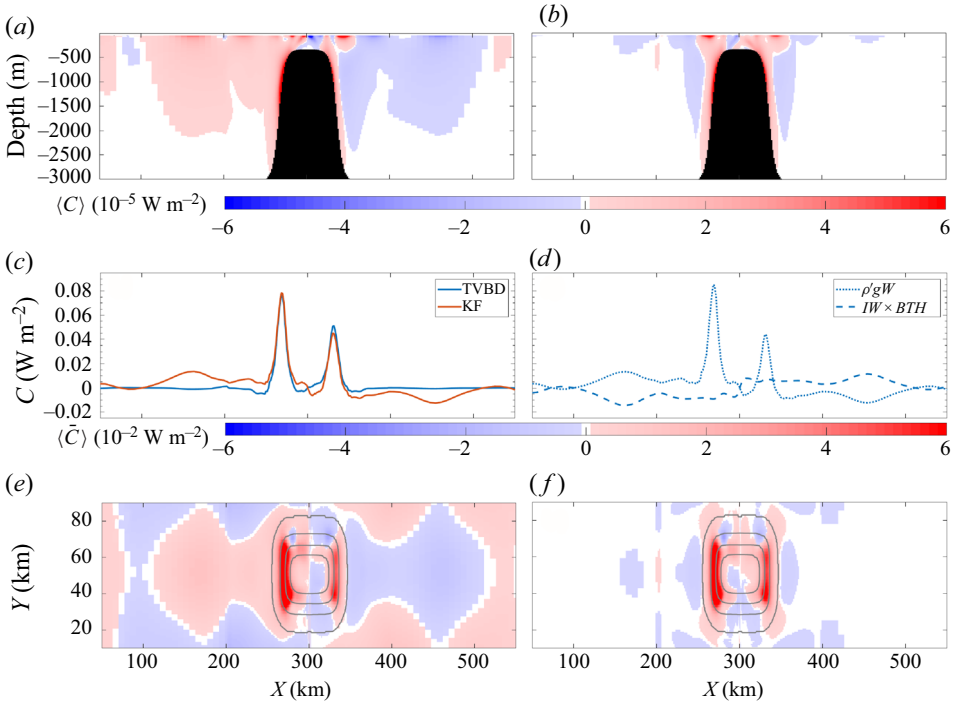

Figure 9. (*a*,*b*) Show the time-averaged conversion rate ($\langle C\rangle$) using KF and TVBD at the transect $Y = 50$ km. The time-averaged depth-integrated conversion rate ($\langle\bar{C}\rangle$) at the transect $Y = 50$ km for both methods can be seen in (*c*); while the components of TVBD are shown in panel (*d*). The time-averaged depth-integrated conversion rate for the whole domain can be seen in panels (*e*) and (*f*) using KF and TVBD, respectively. Bathymetry contours are spaced at −300, −500, −1000, −2000 and −2900 m in (*e*,*f*).

the ocean bottom is not completely flat near the continental shelf break or ridges so residual conversion may be retained in the topographic conversion term leading to a potential overestimate/underestimate of total topographic conversion.

To better understand the role of $IW \times BTH$ we can decompose the tidal average using Leibniz's integral rule $\langle IW \times BTH\rangle = -g\int_0^T\int_{z-\delta}^{z}(\partial\rho_b(z',t)/\partial t)\,\mathrm{d}z'\mathrm{d}t = g\int_0^T(\partial\delta/\partial t)\rho_b(z-\delta,t)\,\mathrm{d}t - g\int_0^T(\partial/\partial t)\int_{z-\delta}^{z}\rho_b(z',t)\,\mathrm{d}z'\,\mathrm{d}t$ where the first term on the right-hand side is the net conversion over a tidal cycle, and the second term is zero. In the KF method, $\partial\delta/\partial t = w$; however, in the TVBD method, $\partial\delta/\partial t = w'$ as W is removed from w (figure 6*c*,*g*). With $\gamma(x,y,z,t) = \eta(1-z/H)$ defined as the BT vertical displacement in a system with flat bathymetry, we can infer that $\rho_b(z,t)$ and $\rho_b(z-\delta,t)$ are temporally in phase. For gravitational waves (away from their generation site), $\langle\overline{\rho' gW}\rangle$ and $\langle\overline{IW\times BTH}\rangle$ are at complementary angles; therefore, their cosines cancel each other (Cushman-Roisin & Beckers 2013)

$$\phi_{\rho',w'} + \phi_{\rho_b,W} = \pi, \tag{4.3}$$

and $IW \times BTH$ cancels any conversion induced by $\rho' gW$ over flat bathymetry.

The overall differences in the estimation of C at generation points by the LSY and KF methods are minor (less than 5 % and 10 %, respectively) due to the interaction of BTH with the IWs (figure 8; similar to the residuals in § 4*b*). This overestimation, however, is

Variable	LSY	KF	TVBD
C_{max}, C_{min} [μW m^{-3}]	N/A	122, -1.5	111, -0.5
$[\langle\bar{C}\rangle]_{x=max,min}$ [mW m^{-2}]	13, -0.1	15, -3	14, -1
$\int_0^X \langle\bar{C}\rangle\,\mathrm{d}x$ [W m^{-1}]	140	135	136
Removes residual conversion in temporal analysis	✓	×	✓
Removes residual conversion at IW reflection points	×	×	✓
Provides accurate estimate of conversion at the generation site	×	×	✓
Provides conversion details through the water column	×	✓	✓

Table 1. Comparison of methods for estimating BT–BC conversion; C_{max} and C_{min} are the maximum and minimum conversion during the whole run time at x, z of 331 km, 613 m where the maximum conversion occurs, $[\langle\bar{C}\rangle]_{x=max}$ and $[\langle\bar{C}\rangle]_{x=min}$ are the maximum and minimum values across shore during the entire run time.

compensated by negative C away from the slope as the spatial integrals of C for the LSY, KF and TVBD methods are similar.

In a similar context, Kelly *et al.* (2010) decomposed and removed shoaling IWs (waves become steeper and more nonlinear as they approach the shore) which resembles the role of BTH in this study. This requires discerning the phasing of other phenomena like shoaling IW or BTH. Determining the phase, however, is not trivial since the phase changes as a wave propagates in the system. Phase variation is obvious as the magnitudes of W and ρ' do not vary significantly over the flat bottom part of the domain; yet, there is a meaningful conversion gradient due to $\phi_{\rho',W}$ (figure 8*a*,*c*). Also, the modal decomposition utilizes linear superimposition of unwanted (shoaling) and wanted (local) phenomena which may not hold for nonlinear cases.

4.3. *Extension to 3-D case*

To test the performance of the TVBD method and its extension to a more realistic set-up, we compared the CBD and TVBD results for an idealized ridge case. As shown in figure 9, there is a good agreement between the CBD and TVBD patterns. In the 3-D case, IW reflection and the residual conversion are obvious in the KF method which are removed through the $IW \times BTH$ term (figure 9*b*,*f*). The spatial integral of C over the whole domain of the 3-D ridge is equal to 66.5 and 63.5 MW for the KF and TVBD methods, respectively. The TVBD does not remove all residual C in the 3-D case especially at the flanks of the ridge due to $IW \times IW$ interactions, yet there is still significant improvement in estimates of C, especially through time as tidal averaging is not needed. We believe that incorporation of IW displacements in the definition of ρ_b would remove these regions of residual conversion as well.

5. Conclusion

In this study, we compared BT to BC energy conversion over sloping bottoms using a new time-variant background density method to commonly used methods (LSY and KF) utilizing CBD. Table 1 highlights the (dis)advantages of each method as well as the numerical results for one of the case scenarios. Our method allows for analysis of conversion through time and over depth, while also removing residual conversion. TVBD provides greater analytical detail because the method is derived directly from the governing equations. However, our analysis confirms the effectiveness of other

methods that work for field data where the resolution is limited in time and space for depth-integrated, time-averaged values (similar values of $\int_0^X \langle \bar{C} \rangle \, \mathrm{d}x$ in table 1).

A portion of BT tidal energy is converted to the BC energy over sloping topography due to the phase difference between the BT vertical velocity W and the density perturbation ρ'. The density perturbation is the result of BTH, local acceleration over the sloping bottom and BC oscillations. CBD methods attempt to remove the BTH effects by averaging over tidal cycles. However, these methods suffer from the presence of residual values in C time series although the net tidally averaged C is zero (C_{min} values in table 1 are more negative in KF than TVBD). The need to tidally average limits the utility of CBD methods to time scales longer than a tidal cycle. The TVBD method remedies this issue through an additional term representing the interaction between BTH and IWs. The TVBD method also provides an improvement over modal decomposition methods (Kelly *et al.* 2010) because wave–tide interactions are removed directly through the $IW \times BTH$ term; $IW \times BTH$ emerges in the energy budget equation due to the TVBD profile and improves discrimination between IW generation due to flow over topography vs other mechanisms of BT–BC conversion. Moreover, by removing the effect of BTH, TVBD allows identification of locations with real negative conversion (due to pressure work or turbulent overturning, and not an artefact of interaction terms) as well as topographies with no conversion where IWs are generated at one location and absorbed at another (Zilberman *et al.* 2009; Maas 2011). Removing these interactions also allows for a more efficient evaluation of BT–BC conversion over a tidal cycle, which is not possible using CBD methods since residuals are removed by tidal averaging. The numerical simulations performed in SUNTANS illustrate the improved estimation of BT–BC conversion using the TVBD method. Although the methods compared in this study estimate the BT to BC energy conversion from different perspectives, the value of total conversion over the domain is similar. Although we recognize the necessity to conduct further tests to study the efficiency of TVBD with nonlinear cases such as solitons, this method provides a step forward in our understanding of IW dynamics.

Acknowledgements. We thank S.G. Monismith, O. Fringer and M. Rayson for helpful discussions during the development of this study.

Funding. This work was funded by the National Science Foundation- Division of Ocean Sciences (NSF-OCE grant 1416837) to C Brock Woodson.

Declaration of interests. The authors report no conflict of interest.

Author ORCIDs.
Sorush Omidvar https://orcid.org/0000-0002-1860-6137;
Mohammadreza Davoodi https://orcid.org/0000-0001-6035-1759;
C. Brock Woodson https://orcid.org/0000-0003-1325-3667.

Appendix A

A.1. *Continuity*

Integrating the BT continuity equation (2.8) over the water column depth, applying the boundary condition and adding $(U + V)(\partial z/\partial x) = 0$ yields

$$\int_{-d}^{z} \left(\frac{\partial U}{\partial x} + \frac{\partial V}{\partial y} \right) \mathrm{d}z = - \int_{-d}^{z} \frac{\partial W}{\partial z} \mathrm{d}z$$

$$\implies (z+d)\left(\frac{\partial U}{\partial x}+\frac{\partial V}{\partial y}\right)=-W|_z+W|_{-d}-(U+V)\frac{\partial z}{\partial x}$$

$$\implies W=-\frac{\partial}{\partial x}\left((z+d)U\right)-\frac{\partial}{\partial y}\left((z+d)V\right)\implies W=-\nabla_h\cdot(\boldsymbol{U}_h(d+z))\,. \quad \text{(A1)}$$

A.2. *Kinetic energy budget*

Kinetic energy contains BC, BT and cross-terms (BT–BC). To calculate the BC kinetic energy, we should consider BC as well as the cross-term $\rho_0\boldsymbol{U}\boldsymbol{u'}$ in $\frac{1}{2}\rho_0(\boldsymbol{U}+\boldsymbol{u'})^2$. The effect of ρ' can be dismissed as it is negligible in comparison to ρ_0. The full derivation of E'_K can be found in Kang (2010) and Kang & Fringer (2012). The kinetic energy budget can be summarized as

$$E_K=E_{K_{BC}}+E_{K_{BT-BC}}+E_{K_{BT}} \quad \text{(A2)}$$

$$E'_K=E_{K_{BC}}+E_{K_{BT-BC}}=\tfrac{1}{2}\rho_0(u'^2+v'^2+w^2)+\rho_0(Uu'+Vv') \quad \text{(A3)}$$

$$E_{K_{BT}}=\tfrac{1}{2}\rho_0(U^2+V^2). \quad \text{(A4)}$$

Time averaging the E'_K energy budget and recognizing for a periodic system that $\int_0^T(\partial E'_K/\partial t)\,\mathrm{d}t=[E'_K]_0^T=0$ yields

$$\nabla_{\boldsymbol{h}}\cdot\left\langle\overline{\boldsymbol{u_h}E'_k}+\overline{\boldsymbol{u'_h}EK_{BT-BC}}+\overline{\boldsymbol{u'_h}P'}-\overline{\nu_H\nabla_{\boldsymbol{h}}E'_K}\right\rangle=-\langle\overline{\rho' g w'}\rangle+\langle A_h\rangle-\langle D'\rangle-\langle\overline{\epsilon_K}\rangle, \quad \text{(A5)}$$

with the definitions

$$\epsilon_K=\rho_0\nu_H(\nabla_{\boldsymbol{h}}\boldsymbol{u'_h}\cdot\nabla_{\boldsymbol{h}}\boldsymbol{u'_h})+\rho_0\nu_V\left(\frac{\partial\boldsymbol{u'_h}}{\partial z}\cdot\frac{\partial\boldsymbol{u'_h}}{\partial z}\right)$$

$$+\rho_0\nu_H(\nabla_{\boldsymbol{h}}w\cdot\nabla_{\boldsymbol{h}}w)+\rho_0\nu_V\left(\frac{\partial w}{\partial z}\cdot\frac{\partial w}{\partial z}\right) \quad \text{(A6)}$$

$$A_h=\rho_0H(UA_x+VA_y) \quad \text{(A7)}$$

$$D'=\rho_0C_B(u'u+v'v+w^2)\sqrt{u^2+v^2}\quad\text{at } z=-d. \quad \text{(A8)}$$

In (A5), the left-hand side is the flux (advection of E'_K, advection of EK_{BT-BC}, pressure and dissipation) and the terms on the right-hand side are buoyancy flux conversion, residual unclosed terms, drag and dissipation, respectively.

A.3. *Available potential energy*

In this section, we derive the available potential energy budget (E_A) based on a TVBD from the definition offered by Lorenz (1955) and Winters *et al.* (1995). Hence, (2.11) changes to

$$E_A(x,y,z,t)=g\int_{z-\delta}^{z}\left(\rho(x,y,z,t)-\rho_0-\rho_b(x,y,z',t)\right)\mathrm{d}z'. \quad \text{(A9)}$$

Implementing the new changes in the available potential energy budget

$$\begin{aligned}\frac{\mathrm{D}E_A}{\mathrm{D}t} &= \frac{\partial E_A}{\partial t} + u\frac{\partial E_A}{\partial x} + v\frac{\partial E_A}{\partial y} + w\frac{\partial E_A}{\partial z} + E_A\left(\frac{\partial u}{\partial x} + \frac{\partial v}{\partial y} + \frac{\partial w}{\partial z}\right)\\ &= \frac{\partial\left(g\delta(\rho(x,y,z,t)-\rho_0)\right)}{\partial t} - \frac{\partial\left(g\displaystyle\int_{z-\delta}^{z}\rho_b(x,y,z',t)\,\mathrm{d}z'\right)}{\partial t}\\ &\quad + u\frac{\partial\left(g\delta(\rho(x,y,z,t)-\rho_0)\right)}{\partial x}\\ &\quad - u\frac{\partial\left(g\displaystyle\int_{z-\delta}^{z}\rho_b(x,y,z',t)\,\mathrm{d}z'\right)}{\partial x} + v\frac{\partial\left(g\delta(\rho(x,y,z,t)-\rho_0)\right)}{\partial y}\\ &\quad - v\frac{\partial\left(g\displaystyle\int_{z-\delta}^{z}\rho_b(x,y,z',t)\,\mathrm{d}z'\right)}{\partial y}\\ &\quad + w\frac{\partial\left(g\delta(\rho(x,y,z,t)-\rho_0)\right)}{\partial z} - w\frac{\partial\left(g\displaystyle\int_{z-\delta}^{z}\rho_b(x,y,z',t)\,\mathrm{d}z'\right)}{\partial z}. \end{aligned} \tag{A10}$$

We acknowledge that both ρ and ρ_b are functions of x, y and z as well as t under the TVBD formulation. For the sake of simplicity, we discard x, y and t and only keep the depth to differentiate between z, z' (the independent argument of the integral) and $z-\delta$. So, $\rho(z)$ should be interpreted as $\rho(x,y,z,t)$.

$$\begin{aligned}\frac{\mathrm{D}E_A}{\mathrm{D}t} &= g\left((\rho(z)-\rho_0)\frac{\partial\delta}{\partial t} + \delta\frac{\partial\rho(z)}{\partial t} - \left(-\frac{\partial(z-\delta)}{\partial t}\rho_b(z-\delta) + \int_{z-\delta}^{z}\frac{\partial\rho_b(z')}{\partial t}\mathrm{d}z'\right)\right)\\ &\quad + gu\left((\rho(z)-\rho_0)\frac{\partial\delta}{\partial x} + \delta\frac{\partial\rho(z)}{\partial x} - \left(-\frac{\partial(z-\delta)}{\partial x}\rho_b(z-\delta) + \int_{z-\delta}^{z}\frac{\partial\rho_b(z')}{\partial x}\mathrm{d}z'\right)\right)\\ &\quad + gv\left((\rho(z)-\rho_0)\frac{\partial\delta}{\partial y} + \delta\frac{\partial\rho(z)}{\partial y} - \left(-\frac{\partial(z-\delta)}{\partial y}\rho_b(z-\delta) + \int_{z-\delta}^{z}\frac{\partial\rho_b(z')}{\partial y}\mathrm{d}z'\right)\right)\\ &\quad + gw\left((\rho(z)-\rho_0)\frac{\partial\delta}{\partial z} + \delta\frac{\partial\rho(z)}{\partial z} - \left(\frac{\partial z}{\partial z}\rho_b(z) - \frac{\partial(z-\delta)}{\partial z}\rho_b(z-\delta)\right.\right.\\ &\quad \left.\left. + \int_{z-\delta}^{z}\frac{\partial\rho_b(z')}{\partial z}\mathrm{d}z'\right)\right)\\ &= g(\rho(z)-\rho_0)\frac{\mathrm{D}\delta}{\mathrm{D}t} + g\delta\frac{\mathrm{D}\rho(z)}{\mathrm{D}t} - g\rho_b(z-\delta)\left(\frac{\mathrm{D}\delta}{\mathrm{D}t} - w\right) - gw\rho_b(z)\\ &\quad - g\int_{z-\delta}^{z}\frac{\partial\rho_b(z')}{\partial t}\mathrm{d}z' - gu\int_{z-\delta}^{z}\frac{\partial\rho_b(z')}{\partial x}\mathrm{d}z' - gv\int_{z-\delta}^{z}\frac{\partial\rho_b(z')}{\partial y}\mathrm{d}z'. \end{aligned} \tag{A11}$$

Using the density transport equation, $\partial\rho/\partial t + \boldsymbol{u}\cdot\nabla\rho = \partial(\kappa_h(\partial\rho/\partial x))/\partial x + \partial(\kappa_h(\partial\rho/\partial y))/\partial y + \partial(\kappa_v(\partial\rho/\partial z))/\partial z$, we can simplify (A11) further:

$$\frac{\mathrm{D}E_A}{\mathrm{D}t} = g\left(\rho(z)-\rho_0\right)\frac{\mathrm{D}\delta}{\mathrm{D}t} - gw\rho_b(z) - g\int_{z-\delta}^{z}\frac{\partial\rho_b(z')}{\partial t}\mathrm{d}z' - g\rho_b(z-\delta)\left(\frac{\mathrm{D}\delta}{\mathrm{D}t}-w\right) + g\delta\left(\frac{\partial\left(\kappa_h\dfrac{\partial\rho}{\partial x}\right)}{\partial x} + \frac{\partial\left(\kappa_h\dfrac{\partial\rho}{\partial y}\right)}{\partial y} + \frac{\partial\left(\kappa_v\dfrac{\partial\rho}{\partial z}\right)}{\partial z}\right). \tag{A12}$$

By definition, $\rho_b(z-\delta) = \rho(z) - \rho_0$. Therefore, (A12) can be simplified even further as:

$$\begin{aligned}\frac{\mathrm{D}E_A}{\mathrm{D}t} &= g\left(\rho(z)-\rho_0\right)\frac{\mathrm{D}\delta}{\mathrm{D}t} - gw\rho_b(z) - g\int_{z-\delta}^{z}\frac{\partial\rho_b(z')}{\partial t}\mathrm{d}z' - g\left(\rho(z)-\rho_0\right)\left(\frac{\mathrm{D}\delta}{\mathrm{D}t}-w\right)\\ &\quad + g\delta\left(\frac{\partial\left(\kappa_h\dfrac{\partial\rho}{\partial x}\right)}{\partial x} + \frac{\partial\left(\kappa_h\dfrac{\partial\rho}{\partial y}\right)}{\partial y} + \frac{\partial\left(\kappa_v\dfrac{\partial\rho}{\partial z}\right)}{\partial z}\right)\\ &= gw\rho'(z) - g\int_{z-\delta}^{z}\frac{\partial\rho_b(z')}{\partial t}\mathrm{d}z' + \epsilon_A,\end{aligned} \tag{A13}$$

with

$$\epsilon_A = g\delta\left(\frac{\partial\left(K_h\dfrac{\partial\rho}{\partial x}\right)}{\partial x} + \frac{\partial\left(K_h\dfrac{\partial\rho}{\partial y}\right)}{\partial y} + \frac{\partial\left(K_v\dfrac{\partial\rho}{\partial z}\right)}{\partial z}\right). \tag{A14}$$

Integrating (A13) over the water column depth gives

$$\overline{\frac{\partial E_A}{\partial t}} + \overline{u\frac{\partial E_A}{\partial x}} + \overline{v\frac{\partial E_A}{\partial y}} + \overline{w\frac{\partial E_A}{\partial z}} = \overline{gw\rho'(z)} - \overline{g\int_{z-\delta}^{z}\frac{\partial\rho_b(z')}{\partial t}\mathrm{d}z'} + \overline{\epsilon_A}. \tag{A15}$$

Similar to E'_K, tidally averaging E_A yields

$$\left\langle\overline{u\frac{\partial E_A}{\partial x}}\right\rangle + \left\langle\overline{v\frac{\partial E_A}{\partial y}}\right\rangle + \left\langle\overline{w\frac{\partial E_A}{\partial z}}\right\rangle = \left\langle\overline{gw\rho'(z)}\right\rangle - \left\langle\overline{g\int_{z-\delta}^{z}\frac{\partial\rho_b(z')}{\partial t}\mathrm{d}z'}\right\rangle + \langle\overline{\epsilon_A}\rangle\,. \tag{A16}$$

By adding the BC kinetic energy to the available potential energy, the conversion term of $\langle\overline{g\rho'w}\rangle - \langle\overline{g\rho'w'}\rangle - \langle\overline{g\int_{z-\delta}^{z}(\partial\rho_b(z')/\partial t)\,\mathrm{d}z'}\rangle = \langle\overline{g\rho'W}\rangle - \langle\overline{g\int_{z-\delta}^{z}(\partial\rho_b(z')/\partial t)\,\mathrm{d}z'}\rangle$ is obtained.

To derive (A16), no specific assumption was made regarding the variation of background density ρ_b with time and any arbitrary function of z and t can be assigned to it. To account for BTH, ρ_b is defined to heave up and down barotropically. To do so, we use $\rho_b(z-\gamma)$ instead of $\rho_b(z)$ where $\gamma(x,y,z,t)$ is the BT vertical displacement in a system with flat bathymetry defined as

$$\gamma(x,y,z,t) = \eta\left(1-\frac{z}{H}\right). \tag{A17}$$

Variable	Description	Variable	Description
ρ_0, ρ_b, ρ'	Reference, background and perturbation density	P_0, P_b, P'	Reference, background and perturbation pressure
f,ω	Coriolis and wave frequency	C_B	Ocean bottom drag coefficient
κ_H, κ_V	Horizontal and vertical diffusion	ν_H, ν_V	Horizontal and vertical viscosity
η, $-d$	Ocean surface and bottom	H	Water column depth
U, V, W	BT velocity	u', v', w'	BC velocity
E_K, E'_K	Total and BC kinetic energy	ϵ_K	BC Dissipation
D'	Drag in BC kinetic energy budget	ϵ_A	Diffusion in E_A budget
$\phi_{a,b}$	Phase difference between a and b	A_h	Unclosed term in energy budget
E_B, E_A, E_P	Min, available and perturbed potential energy	θ_{IW}, θ_B	Angle of IW and ocean bottom with horizon
$\bar{\psi}$, $\langle\psi\rangle$	$\int_{-d}^{\eta}\psi\,\mathrm{d}z'$, $\frac{1}{T}\int_0^T\psi\,\mathrm{d}t'$	β_1, β_2	Steepness and tidal excursion
γ,δ	BT and IW Vertical displacement		

Table 2. Variables and symbols used in the paper.

Case	1	2	3
C_d	0.005	0.005	0.005
L (km)	150	400	600
Δx (m)	30	160	300–1500
Δt (s)	15	15	15
N_k	200	400	400
Δz_{min}, Δz_{max} (m)	0.76, 2.6	1.7, 20.2	1.7, 20.2
h_0, H_0 (m)	30, 300	300, 3000	300, 3000
L_s (m), x_{mid} (km)	7500, 130	750, 325	750, 300
U_0 (m s^{-1})	0.04	0.03	0.04
η_{max} (m)	0.5	1.5	1.5
θ_B, θ_{IW}	0.17, 0.021	0.12, 0.046	0.18, 0.070
β_1	8	2.6	2.58
C_{max} Location (X (km), Z (m))	130, 156.6	330,787	269, 1699

Table 3. Case details show bottom drag coefficient (C_d), domain length (L), horizontal and temporal resolutions (ΔX and Δt), number of vertical layers (N_k), minimum and maximum layer thickness (Δz_{min} and Δz_{max}), minimum and maximum bathymetry depth (h_0 and H_0), bathymetric shape constants (L_s, X_{mid}), tidal current velocity at the ocean-side boundary (U_0) and maximum of the tidal height (η_{max}).

A.4. *Symbols and parameters*

The variables used in this study and the case scenario details can be found in tables 2 and 3, respectively.

References

Baines, P.G. 1974 The generation of internal tides over steep continental slopes. *Phil. Trans. R. Soc. Lond.* A **277** (1263), 27–58.

Baines, P.G. 1982 On internal tide generation models. *Deep-Sea Res.* A **29** (3), 307–338.

Bell, T.H. 1975 Topographically generated internal waves in the open ocean. *J. Geophys. Res.* **80** (3), 320–327.

Carter, G.S., Merrifield, M.A., Becker, J.M., Katsumata, K., Gregg, M.C., Luther, D.S., Levine, M.D., Boyd, T.J. & Firing, Y.L. 2008 Energetics of M 2 barotropic-to-baroclinic tidal conversion at the Hawaiian Islands. *J. Phys. Oceanogr.* **38** (10), 2205–2223.

Cushman-Roisin, B. & Beckers, J.-M. 2013 Introduction to geophysical fluid dynamics.

Dossmann, Y., Pollet, F., Odier, P. & Dauxois, T. 2017 Mixing and formation of layers by internal wave forcing. *J. Geophys. Res.* **122** (12), 9906–9917.

Egbert, G.D. & Ray, R.D. 2000 Significant dissipation of tidal energy in the deep ocean inferred from satellite altimeter data. *Nature* **405** (6788), 775–778.

Fringer, O.B., Gerritsen, M. & Street, R.L. 2006 An unstructured-grid, finite-volume, nonhydrostatic, parallel coastal ocean simulator. *Ocean Model.* **14** (3), 139–173.

Garrett, C. & Kunze, E. 2007 Internal tide generation in the deep ocean. *Annu. Rev. Fluid Mech.* **39**, 57–87.

Garrett, C. & Munk, W. 1979 Internal waves in the ocean. *Annu. Rev. Fluid Mech.* **11** (1), 339–369.

Gerkema, T., Lam, F.P.A. & Maas, L.R.M. 2004 Internal tides in the Bay of Biscay: conversion rates and seasonal effects. *Deep-Sea Res. II* **51** (25–26 Special Issue), 2995–3008.

Gill, A.E. 1982 Waves of large horizontal scale: Normal modes. In *Atmosphere–Ocean Dynamics* (ed. W. L. Donn), pp. 159–162. Academic Press.

Holloway, P.E. & Merrifield, M.A. 1999 Internal tide generation by seamounts, ridges, and islands. *J. Geophys. Res.* **104** (C11), 25937–25951.

Jachec, S.M., Fringer, O.B., Street, R.L. & Gerritsen, M.G. 2007 Effects of grid resolution on the simulation of internal tides. *Intl J. Offshore Polar Engng* **17** (2), 432–438.

Kang, D. 2010 Energetics and dynamics of internal tides in monterey bay using numerical simulations a dissertation submitted to the department of civil and environmental engineering and the committee on graduate studies of Stanford University in partial fulfillment of. PhD thesis, Stanford university.

Kang, D. & Fringer, O. 2010 On the calculation of available potential energy in internal wave fields. *J. Phys. Oceanogr.* **40** (11), 2539–2545.

Kang, D. & Fringer, O. 2012 Energetics of barotropic and baroclinic tides in the Monterey Bay area. *J. Phys. Oceanogr.* **42** (2), 272–290.

Kelly, S.M. & Nash, J.D. 2010 Internal-tide generation and destruction by shoaling internal tides. *Geophys. Res. Lett.* **37** (23), L23611.

Kelly, S.M., Nash, J.D. & Kunze, E. 2010 Internal-tide energy over topography. *J. Geophys. Res.* **115** (6), C06014.

Klymak, J.M., Moum, J.N., Nash, J.D., Kunze, E., Girton, J.B., Carter, G.S., Lee, C.M., Sanford, T.B. & Gregg, M.C. 2006 An estimate of tidal energy lost to turbulence at the Hawaiian ridge. *J. Phys. Oceanogr.* **36** (6), 1148–1164.

Kunze, E., Rosenfeld, L.K., Carter, G.S. & Gregg, M.C. 2002 Internal waves in Monterey Submarine Canyon. *J. Phys. Oceanogr.* **32** (6), 1890–1913.

Kurapov, A.L., Egbert, G.D., Allen, J.S., Miller, R.N., Erofeeva, S.Y. & Kosro, P.M. 2003 The M2 internal tide off Oregon: inferences from data assimilation. *J. Phys. Oceanogr.* **33** (8), 1733–1757.

Lamb, K.G. 2007 Energy and pseudoenergy flux in the internal wave field generated by tidal flow over topography. *Cont. Shelf Res.* **27** (9), 1208–1232.

Lien, R.-C., Henyey, F., Ma, B. & Yang, Y.J. 2014 Large-amplitude internal solitary waves observed in the Northern South China Sea: properties and energetics. *J. Phys. Oceanogr.* **44** (4), 1095–1115.

Llewellyn, S., Stefan, G. & Young, W.R. 2002 Conversion of the barotropic tide. *J. Phys. Oceanogr.* **32** (5), 1554–1566.

Lorenz, E.N. 1955 Available potential energy and the maintenance of the general circulation. *Tellus* **7** (2), 157–167.

Lu, Y., Wright, D.G. & Brickman, D. 2001 Internal tide generation over topography: experiments with a free-surface z-level ocean model. *J. Atmos. Ocean. Technol.* **18** (6), 1076–1091.

Maas, L.R.M. 2011 Topographies lacking tidal conversion. *J. Fluid Mech.* **684**, 5–24.

MacCready, P. & Giddings, S.N. 2016 The mechanical energy budget of a regional ocean model. *J. Phys. Oceanogr.* **46** (9), 2719–2733.

MELLOR, G.L. & YAMADA, T. 1982 Development of a turbulence closure model for geophysical fluid problems. *Rev. Geophys.* **20** (4), 851–875.

MERRIFIELD, M.A. & HOLLOWAY, P.E. 2002 Model estimates of M2 internal tide energetics at the Hawaiian Ridge. *J. Geophys. Res.* **107** (C8), 3179.

MERRIFIELD, M.A., HOLLOWAY, P.E. & JOHNSTON, T.M.S. 2001 The generation of internal tides at the Hawaiian ridge. *Geophys. Res. Lett.* **28** (4), 559–562.

MOUM, J.N., KLYMAK, J.M., NASH, J.D., PERLIN, A. & SMYTH, W.D. 2007 Energy transport by nonlinear internal waves. *J. Phys. Oceanogr.* **37** (7), 1968–1988.

MÜLLER, M. 2013 On the space-and time-dependence of barotropic-to-baroclinic tidal energy conversion. *Ocean Model.* **72**, 242–252.

MUNK, W. & WUNSCH, C. 1998 Abyssal recipes II: energetics of tidal and wind mixing. *Deep-Sea Res. I* **45** (12), 1977–2010.

NASH, J.D., SHROYER, E.L., KELLY, S.M., INALL, M.E., DUDA, T.F., LEVINE, M.D., JONES, N.L. & MUSGRAVE, R.C. 2012 Are any coastal internal tides predictable? *Oceanography* **25** (2), 80–95.

NELKO, V., SAHA, A. & CHUA, V.P. 2014 On the tidally driven circulation in the South China Sea: modeling and analysis. *Ocean Dyn.* **64** (3), 413–428.

PALMER, M.R., STEPHENSON, G.R., INALL, M.E., BALFOUR, C., DÜSTERHUS, A. & GREEN, J.A.M. 2015 Turbulence and mixing by internal waves in the Celtic Sea determined from ocean glider microstructure measurements. *J. Mar. Syst.* **144**, 57–69.

PICKERING, A., ALFORD, M., NASH, J., RAINVILLE, L., BUIJSMAN, M., KO, D.S. & LIM, B. 2015 Structure and variability of internal tides in Luzon Strait. *J. Phys. Oceanogr.* **45** (6), 1574–1594.

POLLMANN, F., NYCANDER, J., EDEN, C. & OLBERS, D. 2019 Resolving the horizontal direction of internal tide generation. *J. Fluid Mech.* **864**, 381–407.

RATTRAY, M. JR. 1960 On the coastal generation of internal tides. *Tellus* **12** (1), 54–62.

SCOTTI, A., BEARDSLEY, R. & BUTMAN, B. 2006 On the interpretation of energy and energy fluxes of nonlinear internal waves: an example from Massachusetts Bay. *J. Fluid Mech.* **561**, 103–112.

VENAYAGAMOORTHY, S.K. & FRINGER, O.B. 2005 Nonhydrostatic and nonlinear contributions to the energy flux budget in nonlinear internal waves. *Geophys. Res. Lett.* **32** (15), L15603.

WINTERS, K.B., LOMBARD, P.N., RILEY, J.J. & D'ASARO, E.A. 1995 Available potential energy and mixing in density-stratified fluids. *J. Fluid Mech.* **289**, 115–128.

XU, M. & CHUA, V.P. 2016 A numerical study on circulation and volume transport in Singapore coastal waters. *J. Hydro-Environ. Res.* **12**, 70–90.

ZHANG, Z., FRINGER, O.B. & RAMP, S.R. 2011 Three-dimensional, nonhydrostatic numerical simulation of nonlinear internal wave generation and propagation in the South China Sea. *J. Geophys. Res.* **116** (C5), C05022.

ZILBERMAN, N.V., BECKER, J.M., MERRIFIELD, M.A. & CARTER, G.S. 2009 Model estimates of M2 internal tide generation over mid-Atlantic ridge topography. *J. Phys. Oceanogr.* **39** (10), 2635–2651.

ZILBERMAN, N.V., MERRIFIELD, M.A., CARTER, G.S., LUTHER, D.S., LEVINE, M.D. & BOYD, T.J. 2011 Incoherent nature of M2 internal tides at the Hawaiian ridge. *J. Phys. Oceanogr.* **41** (11), 2021–2036.